



NAVAL POSTGRADUATE SCHOOL

MONTEREY, CALIFORNIA

THESIS

**DESIGN OF HIGH POWER FELS AND THE EFFECTS OF
DIFFRACTION ON DETUNING IN AN FEL OSCILLATOR**

by

Michael Jayson Price

December 2015

Thesis Advisor:
Second Reader:

Joseph Blau
Keith Cohn

Approved for public release; distribution is unlimited

THIS PAGE INTENTIONALLY LEFT BLANK

REPORT DOCUMENTATION PAGE			Form Approved OMB No. 0704-0188	
Public reporting burden for this collection of information is estimated to average 1 hour per response, including the time for reviewing instruction, searching existing data sources, gathering and maintaining the data needed, and completing and reviewing the collection of information. Send comments regarding this burden estimate or any other aspect of this collection of information, including suggestions for reducing this burden to Washington headquarters Services, Directorate for Information Operations and Reports, 1215 Jefferson Davis Highway, Suite 1204, Arlington, VA 22202-4302, and to the Office of Management and Budget, Paperwork Reduction Project (0704-0188) Washington DC 20503.				
1. AGENCY USE ONLY (Leave Blank)	2. REPORT DATE 12-18-2015	3. REPORT TYPE AND DATES COVERED Master's Thesis 10-01-2013 to 12-18-2015		
4. TITLE AND SUBTITLE DESIGN OF HIGH POWER FELS AND THE EFFECTS OF DIFFRACTION ON DETUNING IN AN FEL OSCILLATOR		5. FUNDING NUMBERS		
6. AUTHOR(S) Michael Jayson Price				
7. PERFORMING ORGANIZATION NAME(S) AND ADDRESS(ES) Naval Postgraduate School Monterey, CA 93943		8. PERFORMING ORGANIZATION REPORT NUMBER		
9. SPONSORING / MONITORING AGENCY NAME(S) AND ADDRESS(ES) N/A		10. SPONSORING / MONITORING AGENCY REPORT NUMBER		
11. SUPPLEMENTARY NOTES The views expressed in this document are those of the author and do not reflect the official policy or position of the Department of Defense or the U.S. Government. IRB Protocol Number: N/A.				
12a. DISTRIBUTION / AVAILABILITY STATEMENT Approved for public release; distribution is unlimited		12b. DISTRIBUTION CODE		
13. ABSTRACT (maximum 200 words) In experiments going back to the first free electron laser (FEL) oscillator at Stanford, the measured width of the desynchronization curve is often significantly greater than predicted by theory and two-dimensional (2D) simulations in (z, t) . The results of new four-dimensional (4D) simulations in (x, y, z, t) show that this difference can be explained by the effects of diffraction. When the light is artificially constrained to remain in the cavity fundamental mode, 2D and 4D simulations give similar results, but when the light is allowed to self-consistently develop higher-order modes, the 4D simulations give different results that agree better with experiments. The results of new 4D simulations also show the effects of emittance versus electron beam energy and mirror shift versus mirror tilt on extraction. Analysis of these results examine the robustness of FEL designs.				
14. SUBJECT TERMS FEL, emittance, energy spread, mirror tilt, mirror shift			15. NUMBER OF PAGES 63	
			16. PRICE CODE	
17. SECURITY CLASSIFICATION OF REPORT Unclassified	18. SECURITY CLASSIFICATION OF THIS PAGE Unclassified	19. SECURITY CLASSIFICATION OF ABSTRACT Unclassified	20. LIMITATION OF ABSTRACT UU	

NSN 7540-01-280-5500

Standard Form 298 (Rev. 2-89)
Prescribed by ANSI Std. Z39-18

THIS PAGE INTENTIONALLY LEFT BLANK

Approved for public release; distribution is unlimited

**DESIGN OF HIGH POWER FELS AND THE EFFECTS OF DIFFRACTION ON
DETUNING IN AN FEL OSCILLATOR**

Michael Jayson Price
Lieutenant, United States Navy
B.S., Marshall University, 2008

Submitted in partial fulfillment of the
requirements for the degree of

MASTER OF SCIENCE IN APPLIED PHYSICS

from the

**NAVAL POSTGRADUATE SCHOOL
December 2015**

Author: Michael Jayson Price

Approved by: Joseph Blau
Thesis Advisor

Keith Cohn
Second Reader

Kevin Smith
Chair, Department of Physics

THIS PAGE INTENTIONALLY LEFT BLANK

ABSTRACT

In experiments going back to the first free electron laser (FEL) oscillator at Stanford, the measured width of the desynchronism curve is often significantly greater than predicted by theory and two-dimensional (2D) simulations in (z, t) . The results of new four-dimensional (4D) simulations in (x, y, z, t) show that this difference can be explained by the effects of diffraction. When the light is artificially constrained to remain in the cavity fundamental mode, 2D and 4D simulations give similar results, but when the light is allowed to self-consistently develop higher-order modes, the 4D simulations give different results that agree better with experiments. The results of new 4D simulations also show the effects of emittance versus electron beam energy and mirror shift versus mirror tilt on extraction. Analysis of these results examine the robustness of FEL designs.

THIS PAGE INTENTIONALLY LEFT BLANK

Table of Contents

1	Introduction	1
1.1	A Brief History	1
1.2	Overview of Thesis Research	1
1.3	Outline	2
2	Theory of Free Electron Lasers	3
2.1	Component Description of an Energy-Recovery Linac Free Electron Laser .	3
2.2	FEL Resonance Condition.	4
2.3	The Pendulum Equation	5
2.4	The Wave Equation	9
2.5	Pulse Lethargy and the Detuning Curve	14
3	FEL Simulation Codes Overview	17
4	Design of High Power FELs	21
5	Results	25
5.1	Jefferson Laboratory FEL	25
5.2	Stanford FEL	31
5.3	Emittance Versus Energy Spread	35
5.4	Mirror Shift and Tilt	38
6	Conclusion	41
	List of References	43
	Initial Distribution List	45

THIS PAGE INTENTIONALLY LEFT BLANK

List of Figures

Figure 2.1	Diagram of the components of an Energy Recovery Linac FEL	3
Figure 2.2	Evolution of electrons through the undulator in phase space.	9
Figure 2.3	Depiction of pulse lethargy with the electron pulse in red and the optical pulse in blue.	14
Figure 2.4	Example of a detuning curve.	15
Figure 3.1	First sample graphical output from 4D model.	18
Figure 3.2	Second sample graphical output from 4D model.	19
Figure 4.1	Emittance is defined by the area of the electron bunch in phase space, particle angle (x') versus particle position (x), from [18]	22
Figure 4.2	Mirror Shift (Δy_m)	22
Figure 4.3	Mirror Tilt ($\Delta \theta_m$)	23
Figure 5.1	Modeled desynchronism curve (extraction η versus dimensionless desynchronism value d) for Jefferson Laboratory 14 kW FEL using the NPS 2D model (blue) and the new 4D model (red)	26
Figure 5.2	Optical wavefront depiction for $d = 0.02$. Top: optical amplitude $ a $ versus z at $x = y = 0$. Bottom: optical amplitude $ a $ versus (x, y) at $z = 0$	27
Figure 5.3	Optical wavefront depiction for $d = 0.2$. Top: optical amplitude $ a $ versus z at $x = y = 0$. Bottom: optical amplitude $ a $ versus (x, y) at $z = 0$	27
Figure 5.4	Adjusted desynchronism curve for Jefferson Laboratory 14 kW FEL. For the 4D model (red), the cavity mirrors are now positioned just outside the undulatory, forcing the optical wavefront to remain primarily in the fundamental mode	29

Figure 5.5	Adjusted optical wavefront depiction for $d = 0.02$. Top: optical amplitude $ a $ versus z at $x = y = 0$. Bottom: optical amplitude $ a $ versus (x, y) at $z = 0$	30
Figure 5.6	Adjusted optical wavefront depiction for $d = 0.2$. Top: optical amplitude $ a $ versus z at $x = y = 0$. Bottom: optical amplitude $ a $ versus (x, y) at $z = 0$	30
Figure 5.7	Modeled desynchronism curve for Stanford FEL	32
Figure 5.8	Experimental desynchronism curve for Stanford FEL, from [19]	33
Figure 5.9	Optical wavefront depiction for $d = 0.004$	34
Figure 5.10	Optical wavefront depiction for $d = 0.06$	34
Figure 5.11	Extraction (η) for emittance ($\epsilon_{x,y}$) versus energy spread ($\Delta\gamma/\gamma$) for a generic oscillator	35
Figure 5.12	Optical field amplitude and optical power spectrum for $\epsilon_{x,y} = 10\mu\text{m}$ and $\Delta\gamma/\gamma = 0\%$	37
Figure 5.13	Optical field amplitude and optical power spectrum for $\epsilon_{x,y} = 5\mu\text{m}$ and $\Delta\gamma/\gamma = 0\%$	38
Figure 5.14	Extraction (η) for mirror shift (Δy_m) versus mirror tilt ($\Delta\theta_m$) for a generic oscillator	39

List of Tables

Table 5.1	Jefferson Laboratory FEL Oscillator Parameters, from [17]	26
Table 5.2	Stanford FEL Oscillator Parameters, from [19]	31
Table 5.3	Generic FEL Oscillator parameters, from [17]	36

THIS PAGE INTENTIONALLY LEFT BLANK

List of Acronyms and Abbreviations

DE	Directed Energy
FEL	Free Electron Laser
FWHM	Full Width at Half Maximum
INP	Innovative Naval Prototype
linac	Linear Accelerator
NPS	Naval Postgraduate School
ONR	Office of Naval Research
RF	Radio Frequency
rms	Root Mean Square
SRF	Superconducting Radio Frequency
SSL	Solid State Laser
USN	United States Navy
2D	Two-Dimensional
3D	Three-Dimensional
4D	Four-Dimensional

THIS PAGE INTENTIONALLY LEFT BLANK

Acknowledgments

It would be a mistake to think that I could thank everyone who helped me along my academic career, so I will focus on my time during this thesis. First of all, I would like to thank the Directed Energy Group at NPS (Dr. Blau, Dr. Cohn, Dr. Colson, Dr. Pogue, and Raquel Herold). I have learned a tremendous amount during my two years with them and they have provided more than their fair share of encouragement. They have renewed my love of academia and research and, for that, I am eternally grateful. I would also like to thank my family for their continued support and encouragement. They have always been there for me and continue to do so. Finally, I would like to thank my wife for enduring my endless rants concerning this work and the many sleepless nights spent thinking and working. She has supported me throughout my career and I would not be here without her.

THIS PAGE INTENTIONALLY LEFT BLANK

CHAPTER 1:

Introduction

1.1 A Brief History

The first free electron laser (FEL) was built at Stanford University and lased in 1976 [1]. This FEL was initially proposed by Madey [2] in 1971 and was based on initial theory and experiments by Motz [3], [4]. Stanford then went on to build and operate the first oscillator FEL in 1977 [5]. Since 1976, FELs have been established across the world [6]–[8] with varying wavelengths and power levels. The most powerful FEL was operated at Jefferson Lab in 2001 [9] with an average power of 14kW as part of a United States Navy (USN) program to design and build a MW class FEL for ship defense. The National Academy of Sciences [10] created a report in 2009 detailing the issues involved in the design of a MW class FEL. The Office of Naval Research (ONR) funded an Innovative Naval Prototype (INP) in 2010 with the goal of designing a prototype for a 100kW FEL. Boeing was selected for this project; however, it was canceled in 2012 as the Navy decided to focus on solid state lasers (SSL) for their near term deployment capabilities.

For Naval applications, directed energy (DE) weapons represent an opportunity to gain a significant advantage in both offensive and defensive capabilities. A SSL has already been deployed on a surface combatant; however, SSLs are limited in power and to a specific wavelength. Previous research at Naval Postgraduate School (NPS) [11] has shown that there are wavelengths outside of the typical SSL operation that enhance propagation through the atmosphere in certain maritime environments. FELs are capable of lasing at these wavelengths with better beam quality and at potentially higher powers that provide better utility in their application. Continuing research regarding FELs is critical for the USN to maintain an advantage in DE weapons.

1.2 Overview of Thesis Research

The DE group at NPS has been developing FEL modeling programs for decades. Recently, it developed a four-dimensional model that follows the evolution of the electron and opti-

cal pulses in the transverse and longitudinal directions. Previous models have been used to simulate FELs, but some discrepancies with comparisons to theoretical and experimental results existed. This thesis work looks at these discrepancies using the new model for the original Stanford FEL and the Jefferson Laboratory 14kW FEL. Research into the design of high power FELs has also been conducted by the DE group, but this was using previous, less sophisticated models. This thesis expands this work by using the new model to determine the robustness of FEL designs.

1.3 Outline

Chapter 2 derives the equations that constitute the base of FEL theory as well as discusses in detail the concepts of pulse lethargy and desynchronism [12], [13]. Chapter 3 discusses the codes used to model FELs and the output from the simulations. Chapter 4 establishes the design parameters of a high power FEL. Chapter 5 lays out the results of the simulations and Chapter 6 discusses the results. Chapter 7 provides a summary of the work as well as a discussion regarding future research.

CHAPTER 2:

Theory of Free Electron Lasers

2.1 Component Description of an Energy-Recovery Linac Free Electron Laser

The components of an energy-recovery linear accelerator (linac) FEL can be seen in Figure 2.1. The first component of an energy-recovery linac FEL is the electron injector. The injector can produce the electrons by different methods (e.g., by a thermionic process or by photoemission). These electrons are produced in a pulse structure with a typical bunch charge (q_b) of 0.1 nC and duration (t_b) of 1 ps. A typical value of the electrons' kinetic energy after the injector is 5 MeV. The electrons are then directed into the linac, which often consists of radio frequency (RF) powered accelerators. For such accelerators, an RF signal is applied to the accelerator cavities to generate an alternating electric field inside them. The alternating electric field continually accelerates the electrons throughout the cavities as the electrons “surf” the RF wave. The electrons in the RF linac are accelerated to a typical energy of 100 MeV.

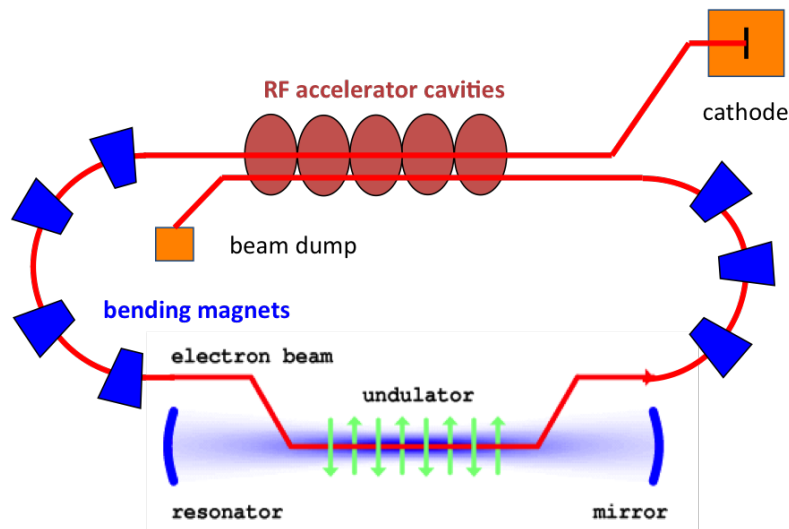


Figure 2.1: Diagram of the components of an Energy Recovery Linac FEL

The electrons are transported between each component via an electron beam line. This line is an evacuated pipe that has a radius of ~ 1 cm and is surrounded by various magnets and detectors. Solenoid and quadrupole magnets are used to focus the beam so that the electrons stay collimated. Dipole magnets are also used to steer the beam at various places.

The next component is the undulator. It is comprised of permanent magnets or electromagnets (with peak magnetic fields of approximately 1 T) arranged in such a way to produce an alternating magnetic field. As the electrons move through the undulator, they wiggle back and forth due to the Lorentz force and emit photons. These photons are often stored in an optical cavity consisting of two mirrors: a highly reflecting (~ 100 % reflective) mirror and a partially transparent ($\sim 1 - 10$ % transparent) mirror. The reflected optical pulse inside the cavity arrives at the undulator at approximately the same time as an electron pulse. The electron pulse then amplifies the optical pulse through the production of additional photons. This process continues over many passes until the gain from the electron pulse equal the losses (due to the partially transparent mirror), which is referred to as saturation. The laser output power depends on the saturated power inside the cavity and the mirror transmission.

The electrons are then recirculated back to the RF linac using dipole magnets. The electrons are now injected 180° out of phase with the RF fields that causes the electrons to decelerate back to near their original injection energy of ~ 5 MeV. This takes energy away from the electrons and transfers it to the RF field (energy recovery). Once the electrons exit the RF linac, they are directed to a beam dump where they impact shielded, conducting material. This method of recycling the electrons greatly enhances the overall “wall plug” efficiency and reduces the generated radiation at the beam dump.

2.2 FEL Resonance Condition

Resonance refers to the condition in which optimum energy exchange occurs. Specifically, Colson [14] describes this as the case where as an electron passes through one undulator period, one wavelength of light passes over it, which is important so that the electron sees the correct electric field as it traverses the undulator. As the electron moves through the undulator, there are two speeds that must be considered: the speed c of the photon and the speed $\beta_z c$ of the electron with

$$\beta_z = \frac{v_z}{c} \approx 1 - \frac{(1 + K^2)}{2\gamma^2}, \quad (2.1)$$

where $K = e\bar{B}\lambda_0/2\pi mc^2$ is the undulator parameter, $\gamma = 1/\sqrt{1 - (v^2/c^2)}$, e is the charge of the electron, \bar{B} is the root mean square field strength over each period, λ_0 is the undulator period, and m is the mass of the electron. The approximation made above will be explained in the next section. The time for an electron to travel one undulator period is $\Delta t = \lambda_0/\beta_z c$. In that time, the photon will move ahead of the electron by a distance of $(c - \beta_z c)\Delta t$, which we equate to the optical wavelength as a condition for resonance where

$$\lambda = (c - \beta_z c)\Delta t = \frac{(1 - \beta_z)\lambda_0}{\beta_z}. \quad (2.2)$$

Placing (2.1) into (2.2) gives the approximate wavelength the FEL will lase at:

$$\lambda \approx \frac{\lambda_0(1 + K^2)}{2\gamma^2}. \quad (2.3)$$

Equation (2.3) shows one of the advantages of an FEL over a solid state laser since the FEL wavelength is tunable by manipulation of either K or γ . The wavelength can also be manipulated by adjusting λ_0 , however this is usually not done as it is easier to manipulate the magnetic field strength or the electron's energy coming out of the accelerator.

2.3 The Pendulum Equation

An electron traveling through a helical undulator along the z -axis is subjected to a magnetic field described as:

$$\vec{B} = B(\cos(k_0 z), \sin(k_0 z), 0),$$

where B is the magnetic field amplitude and $k_0 = 2\pi/\lambda_0$ is the undulator wavenumber. The magnetic and electric fields of the laser are given by

$$\vec{B} = E(\sin(\Psi), \cos(\Psi), 0), \quad (2.4)$$

$$\vec{E} = E(\cos(\Psi), -\sin(\Psi), 0), \quad (2.5)$$

where E is the electric field amplitude (in cgs units), $\Psi = kz - \omega t + \phi$ is the optical phase, $k = 2\pi/\lambda$ is the wavenumber, λ is the optical wavelength, and ω is the optical frequency. The relativistic Lorentz force equations are

$$\frac{d(\gamma\vec{\beta})}{dt} = -\frac{e}{mc}(\vec{E} + \vec{\beta} \times \vec{B}), \quad (2.6)$$

$$\frac{d\gamma}{dt} = -\frac{e}{mc}\vec{\beta} \cdot \vec{E}, \quad (2.7)$$

$$\gamma^{-2} = 1 - \vec{\beta}^2, \quad (2.8)$$

where $\vec{v} = \vec{\beta}c$ is the electron velocity.

The motion of the electron is determined by the combination of the undulator and laser fields. Placing (2.4) and (2.5) into (2.6) gives:

$$\frac{d(\gamma\vec{\beta}_\perp)}{dt} = -\frac{e}{mc}[E(1 - \beta_z)(\cos(\Psi), -\sin(\Psi)) + \beta_z B(-\sin(k_0 z), \cos(k_0 z))], \quad (2.9)$$

$$\frac{d(\gamma\beta_z)}{dt} = -\frac{e}{mc}[E(\beta_x \cos(\Psi) - \beta_y \sin(\Psi)) + B(\beta_x \sin(k_0 z) - \beta_y \cos(k_0 z))], \quad (2.10)$$

where $\vec{\beta}_\perp c$ is the transverse velocity of the electron. Since the electrons are relativistic, $\beta_z \approx 1$, which means (2.9) can be simplified then integrated to

$$\vec{\beta}_\perp = -\frac{K}{\gamma}(\cos(k_0 z), \sin(k_0 z), 0), \quad (2.11)$$

where we assume that the electron is injected into its orbits such that the constants of integration are zero.

To determine the electron's energy exchange with the optical field, we place (2.11) into (2.7) to get

$$\dot{\gamma} = \frac{d\gamma}{dt} = -\frac{e}{mc}E[\beta_x \cos(\Psi) - \beta_y \sin(\Psi)] = \frac{eKE}{\gamma mc} \cos(\zeta + \phi), \quad (2.12)$$

where the electron phase is $\zeta \equiv (k + k_0)z - \omega t$. The variables k_0 , k , and ω are constant which implies that ζ describes the electron's position on the scale of an optical wavelength since $\zeta \propto kz(t)$. When $\cos(\zeta + \phi) > 0$, the electron energy increases and $\dot{\gamma} > 0$; but if $\cos(\zeta + \phi) < 0$, the electron energy decreases and $\dot{\gamma} < 0$ (the desired state as it leads to optical gain). Sufficient energy exchange between the electron and laser beam requires that $\cos(\zeta + \phi)$ not oscillate quickly over time $L/c\beta_z$, where $L = N\lambda_0$ is the length of the undulator and N is the number of undulator periods.

Now, we can define the electron phase velocity as

$$v = \frac{\dot{\zeta}L}{c} = L[(k + k_0)\beta_z - k] = \dot{\zeta},$$

where $(\dots)^\circ = \frac{d(\dots)}{d\tau}$ indicates a derivative taken with respect to dimensionless time $\tau = ct/L$. The parameter τ goes from 0 to 1 as the electron traverses the undulator.

Notice that if $v = 0$, $\beta_z = kc/(k + k_0)$, which is equivalent to the resonance condition (2.2). Thus $v = 0$ corresponds to resonance, where the energy exchange between electrons and light is maximized. Substituting (2.11) into (2.8) gives

$$\beta_z = \left(1 - \frac{1 + K^2}{\gamma^2}\right)^{\frac{1}{2}}.$$

Using the relativistic limit where $\gamma \gg 1$, this can be expanded as

$$\beta_z \approx 1 - \frac{1 + K^2}{2\gamma^2}.$$

Throughout the electron beam, the initial electron phase, $\zeta(0) = \zeta_0 = (k + k_0)z_0 \approx kz_0$, depends on the initial electron position z_0 and is therefore different for each electron. An inspection of (2.12) shows that approximately half of the electrons give energy to the laser beam and the other half take energy from the laser beam. This phenomenon, with half the electrons moving faster and the other half moving slower, causes the electrons to bunch and radiate coherently due to the fact that it occurs on the scale of λ .

If we consider $\dot{v} = L[(k + k_0)\dot{\beta}_z]$ where $\beta_z \approx 1 - (1 + K^2)/2\gamma^2$, and using the resonance condition (2.3) with the assumption $\gamma \gg 1$, then we find that

$$\dot{v} = \frac{4\pi N\dot{\gamma}}{\gamma}. \quad (2.13)$$

Placing (2.12) into (2.13) gives

$$\dot{v} = \dot{\zeta} = |a| \cos(\zeta + \phi), \quad (2.14)$$

where $|a| = 4\pi NeKLE/\gamma^2 mc^2$ is the dimensionless laser field amplitude. Equation (2.14) has the form of the classical pendulum equation and describes how the electrons evolve in phase space (ζ, v) . An inspection of (2.14) shows that when $|a| \gg \pi$ the fields of the laser are strong, which causes the electrons to bunch together; however, if $|a| \ll \pi$ then the fields of the laser are weak and do not cause significant bunching. The electrons follow FEL phase space paths described by

$$v^2 = v_0^2 + 2|a|[\sin(\zeta + \phi) - \sin(\zeta_0 + \phi)],$$

where ζ_0 and v_0 are the initial coordinates of the electron in phase space. Figure 2.2 shows an example of electron evolution in phase space through an undulator. Here, you can see the electrons are introduced at the beginning of the undulator with an initial v . As the electrons progress through the undulator, they begin to evolve in phase space. At the end of the undulator, you can see that the electrons have evolved significantly from their initial v values and are now bunched on the scale of an optical wavelength.

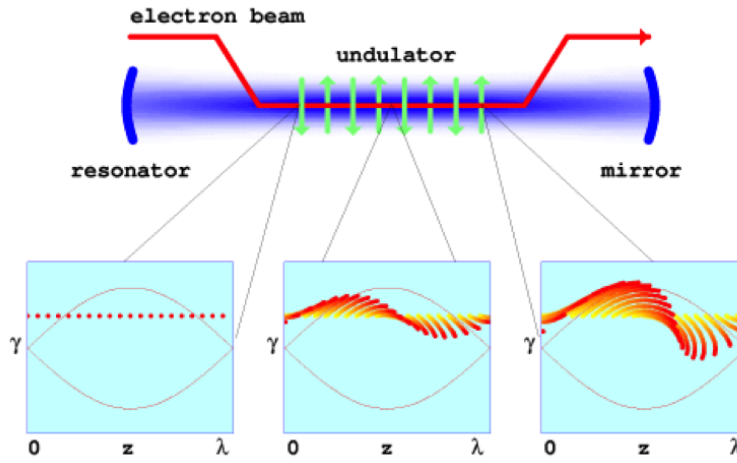


Figure 2.2: Evolution of electrons through the undulator in phase space.

2.4 The Wave Equation

Maxwell's wave equation is

$$\left(\vec{\nabla}^2 - \frac{1}{c^2} \frac{\partial^2}{\partial t^2} \right) \vec{A}(\vec{x}, t) = -\frac{4\pi}{c} \vec{J}_\perp(\vec{x}, t), \quad (2.15)$$

where $\vec{A}(\vec{x}, t)$ is the optical vector potential and J_\perp is the perpendicular component of a current source. The electric and magnetic fields are determined using

$$\vec{E} = -\frac{1}{c} \frac{\partial \vec{A}}{\partial t},$$

$$\vec{B} = \vec{\nabla} \times \vec{A}.$$

For a laser, we can assume the electric field envelope is slowly varying with distance on the scale of an optical wavelength, $\lambda = 2\pi/k$, and in time when compared to the optical period, $2\pi/\omega = \lambda/c$ [14]. Therefore, this motivates us to write the optical vector potential as

$$\vec{A}(\vec{x}, t) = \frac{E(\vec{x}, t)}{k} \hat{e} e^{i\alpha},$$

where $\alpha = kz - \omega t$ is the phase of the carrier wave, $E = |E|e^{i\phi}$ is the complex laser field envelope, and \hat{e} is the polarization vector. Both the amplitude, $|E(\vec{x}, t)|$, and the phase, $\phi(\vec{x}, t)$ of the wave envelope are slowly varying, therefore we can rewrite (14) as

$$\frac{\hat{e} e^{i\alpha}}{k} \left[\vec{\nabla}_{\perp}^2 + 2ik \left(\frac{\partial}{\partial z} + \frac{1}{c} \frac{\partial}{\partial t} \right) \right] E = -\frac{4\pi}{c} \vec{J}_{\perp}, \quad (2.16)$$

where $\nabla_{\perp}^2 = \partial_x^2 + \partial_y^2$.

Using the process of method of characteristics, a coordinate substitution can be made such that

$$E(z, t) = E'(u, t),$$

where $u = z - ct$. Now, we can write

$$\frac{\partial E}{\partial z} = \frac{\partial E'}{\partial u} \frac{\partial u}{\partial z} = \frac{\partial E'}{\partial u}, \quad (2.17)$$

since $\partial u / \partial z = 1$. Likewise,

$$\frac{\partial E}{\partial t} = \frac{\partial E'}{\partial u} \frac{\partial u}{\partial t} + \frac{\partial E'}{\partial t} = (-c) \frac{\partial E'}{u} + \frac{\partial E'}{\partial t}. \quad (2.18)$$

Using (2.17) and (2.18), we can write

$$\frac{\partial E}{\partial z} + \frac{1}{c} \frac{\partial E}{\partial t} = \frac{1}{c} \frac{\partial E'}{\partial t}.$$

Multiplying both sides of (2.16) by $ke^{-i\alpha}\hat{\mathbf{e}}^*$, using the coordinate substitution, and dropping the prime notation now gives the paraxial wave equation

$$\left[\vec{\nabla}_{\perp}^2 + 2ik \left(\frac{1}{c} \frac{\partial}{\partial t} \right) \right] E = -\frac{4\pi k}{c} \vec{J}_{\perp} \cdot \hat{\mathbf{e}}^* e^{-i\alpha}. \quad (2.19)$$

The source current can be written as

$$\vec{J}_{\perp} = -ec \sum_i \vec{\beta}_{\perp} \delta^{(3)}(\vec{x} - \vec{r}_i(t)), \quad (2.20)$$

where $\vec{r}_i(t)$ is the i^{th} electron position at time t . The contribution to the transverse current, from the transverse motion as described in (2.11), is

$$\vec{\beta}_{\perp} = -\frac{K}{\gamma} (\cos(k_0 z), \sin(k_0 z), 0) = \mathbf{Re} \left(-\frac{K}{\gamma} i \hat{\mathbf{e}} e^{-ik_0 z} \right), \quad (2.21)$$

where $\hat{\mathbf{e}} = \frac{1}{\sqrt{2}}(-i, 1, 0)$ for circular polarization from a helical undulator. Substituting (2.21) into (2.20) and then (2.20) into (2.19) gives

$$\left[\vec{\nabla}_{\perp}^2 + \frac{2ik}{c} \frac{\partial}{\partial t} \right] E = -4\pi e K k \rho(\vec{x}, t) \left\langle \frac{e^{-i\zeta}}{\gamma} \right\rangle, \quad (2.22)$$

where $\rho(\vec{x}, t)$ is the local electron density and $\langle e^{-i\zeta}/\gamma \rangle$ represents an average over sample electrons in a volume element dV that is significantly smaller than either the optical or electron pulse, and

$$\int \sum_i \delta^{(3)}(\vec{x} - \vec{r}_i(t)) dV = \rho(\vec{x}, t) dV$$

represents the number of electrons in the volume element.

Here, again, we will use the dimensionless time parameter $\tau = ct/L$ to rewrite (2.22) as

$$\left[\vec{\nabla}_{\perp}^2 + \frac{2ik}{L} \frac{\partial}{\partial \tau} \right] E = -4\pi e K k \rho(\vec{x}, \tau) \left\langle \frac{e^{-i\zeta}}{\gamma} \right\rangle. \quad (2.23)$$

Multiplying (2.23) by $-4\pi NeKL^2/\gamma_0^2 mc^2 k$ now gives the wave equation as

$$\left[\frac{iL}{2k} \vec{\nabla}_{\perp}^2 + \frac{\partial}{\partial \tau} \right] a(\vec{x}, \tau) = -j \langle e^{-i\zeta} \rangle,$$

where $a = |a|e^{i\phi} = 4\pi NeKLE/\gamma_0^2 mc^2$ represents the dimensionless laser field amplitude and the dimensionless FEL current is represented by $j = 8\pi^2 Ne^2 K^2 L^2 \rho/\gamma_0^3 mc^2$ using the assumption that $\gamma \approx \gamma_0$. Defining $\tilde{x} = x(k/2L)^{1/2}$ and $\tilde{y} = y(k/2L)^{1/2}$ allows us to now write the wave equation in completely dimensionless form as

$$\left[-\frac{i}{4} \vec{\nabla}_{\perp}^2 + \frac{\partial}{\partial \tau} \right] a(\vec{x}, \tau) = -j \langle e^{-i\zeta} \rangle,$$

where for simplicity the tildes are dropped and the coordinates (x, y, z, τ) are dimensionless.

The first term in the above equation describes diffraction of the optical field. If we consider the case where the electron and optical beams exactly overlap and the effect of diffraction is small, the wave equation can then be simplified as

$$\dot{a} = -j\langle e^{-i\zeta} \rangle, \quad (2.24)$$

where the coupling between the laser and electron beam is determined by j and the electron bunching by $\langle e^{-i\zeta} \rangle$. For small amounts of bunching, the coupling is small. When the value of $j \lesssim \pi$, the coupling is small but when $j \gg \pi$, the coupling can be large.

Using the fact that $a = |a|e^{i\phi}$, the left side of (2.24) becomes

$$\dot{a} = |\dot{a}|e^{i\phi} + |a|\dot{\phi}ie^{i\phi}. \quad (2.25)$$

Now, placing (2.25) into (2.24) and grouping real and imaginary terms gives

$$|\dot{a}| = -j\langle \cos(\zeta + \phi) \rangle, \quad (2.26)$$

$$\dot{\phi} = \frac{j\langle \sin(\zeta + \phi) \rangle}{|a|}. \quad (2.27)$$

Whether the coupling drives the optical field amplitude $|a|$ or phase ϕ depends on the relative values of ζ and ϕ , as can be seen in (2.26) and (2.27). When electrons bunch, such that $\zeta + \phi \rightarrow \pi$, the value of (2.26) increases. This increase in the dimensionless laser field amplitude in turn causes the electrons to bunch even more via the coupling described in (2.14). As more bunching occurs, this causes ζ and ϕ to become more coupled, thus increasing the value of (2.26). This process is a kind of “feedback” loop between the pendulum and wave equations for the FEL [14]. This loop causes exponential growth initially, until saturation occurs. As the value of $|a|$ increases, the evolution of the electrons in phase space increases. Once the value increases sufficiently, $\zeta + \phi \rightarrow 0$, which causes the electron energy to increase, therefore taking energy from the laser beam. This saturation effect prevents the runaway of the exponential growth in gain.

2.5 Pulse Lethargy and the Detuning Curve

Following the phase space evolution of the electrons through the undulator, as described by (2.14), the electrons enter the undulator unbunched at $\tau = 0$. As the electrons progress through the undulator, they begin to bunch until they reach the end of the undulator, $\tau = 1$, where the electrons have bunched such that they significantly amplify the optical pulse. Recall from the previous discussion on the resonance condition that the photons “slip” ahead of the electrons by a distance of $N\lambda$ over the length of the undulator. This is referred to as the slippage distance [12]. This slippage causes the electrons to amplify the trailing end of the optical pulse, causing the centroid to move slower than c as shown in Figure 2.3. This effect is called lethargy [13] and, over many passes, will cause the optical pulse to fall behind the electron pulse and the amplitude to decay.

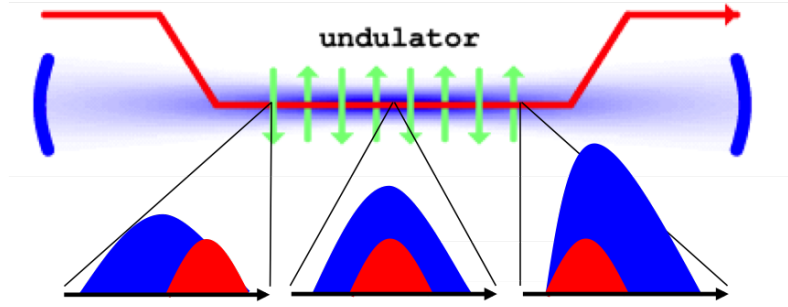


Figure 2.3: Depiction of pulse lethargy with the electron pulse in red and the optical pulse in blue.

To counteract this lethargy effect, the spacing between the mirrors of the optical cavity must be adjusted to shorten the optical cavity. This process is called desynchronization and allows the photon pulse to be advanced after each pass [12]. If the cavity length is shortened by moving one mirror a distance ΔS , then the amount of desynchronize can be characterized by the dimensionless parameter

$$d = \frac{-2\Delta S}{N\lambda}. \quad (2.28)$$

The plot of the electron extraction η vs. d is called the detuning curve, where the extraction

is the output optical power over the input electron beam power; Figure 2.4 gives an example of one. From this example, there is clearly a peak that will provide the most output for the laser, however this region can become unstable in the event of a slight change in the mirror separation. Just beyond the peak is a region that provides much more stability with relatively high output. At large values of d , the extraction goes to zero because the optical pulse advances too far ahead of the electron pulse on each pass [12].

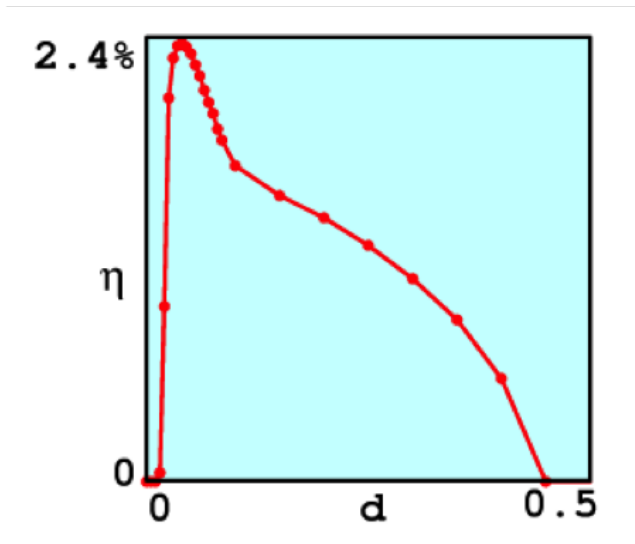


Figure 2.4: Example of a detuning curve.

THIS PAGE INTENTIONALLY LEFT BLANK

CHAPTER 3:

FEL Simulation Codes Overview

The modeling programs used here have been developed by professors J. Blau and W.B. Colson at NPS [15]. All the programs use the dimensionless parameters as previously described. The two-dimensional (2D) program follows the electron and optical pulses in the longitudinal (z) direction in time (t) while the four-dimensional (4D) program follows the pulses in the transverse (x, y) and longitudinal directions in time. The specific 4D model used is for short pulses (optical pulse length comparable to the slippage distance $N\lambda$). In the model, a fourth-order Runge-Kutta method is used to evaluate how the electrons evolve in phase space according to the FEL pendulum equation (2.14). The optical field propagates according to the FEL wave equation (2.24) using a Fourier transform.

Figure 3.1 is an example of the first portion of the graphical output from the 4D model. The shades of blue represent a color scale with the darker blue indicating a lower value than the lighter blue. The bottom row of plots is at the beginning of the first pass and the top row is at the end of the last pass. The middle row of plots shows the evolution over n passes through the undulator. The far left column of plots is labeled $a(x, 0, 0)$ and represents a cross-section of the optical field amplitude versus x where $y = z = 0$. The number in the top right corner of each plot gives the peak value of $|a|$. The electron beam is shown in red and the optical beam in blue. The next column of plots, labeled $a(0, y, 0)$, is nearly identical, showing a cross-section of the field amplitude versus y for $x = z = 0$. The third column of plots, labeled $a(0, 0, z)$, shows the electron pulse and optical field amplitude versus the longitudinal direction z , at $x = y = 0$. Initially, the electron pulse (red) is slightly ahead of the optical pulse (blue), but over the length of the undulator the electron pulse slips behind the optical pulse by $N\lambda$. The final column, labeled $P(0, 0, \nu)$, shows the evolution of the optical power spectrum at $x = y = 0$. The shift in the centroid of the optical spectrum seen here illustrates the phenomenon through which the FEL selects the best wavelength at which to operate, as it evolves from weak fields to saturation [14].

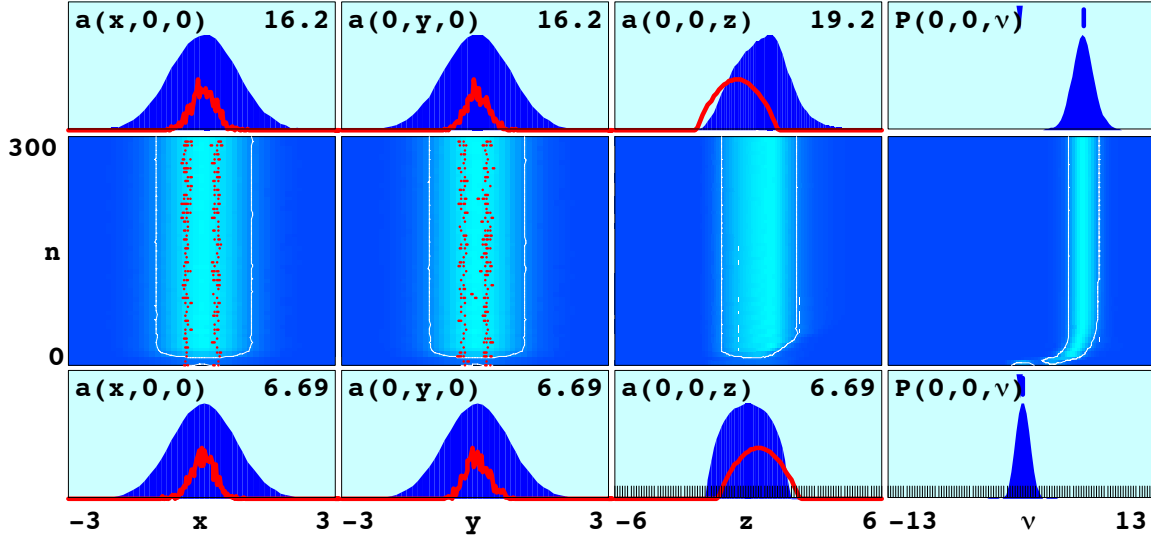


Figure 3.1: First sample graphical output from 4D model.

The second set of plots is shown in Figure 3.2. The top left plot, labeled $f(v,n)$, shows the evolution of the electron phase velocity distribution. The plot next to that shows the final distribution of electrons in phase space and indicates the bunching of the electrons. The two plots in the upper right give a three-dimensional (3D) representation of the optical wavefronts at the left mirror ($\tau = -0.1$) and the right mirror ($\tau = 1.1$). The bottom two plots on the left show the evolution of optical power $P(n)$ and gain $G(n)$ and give their peak values in the upper right. The next plot, labeled $|c(m,p)|$, indicates the modal composition of the optical wavefront. The value of the Hermite-Gaussian coefficients based on the cavity modes are represented by a blue square at each value of (m,p) using the previously mentioned color scale. The last two plots give a 2D representation of the optical wavefront at the left and right mirrors with the peak value indicated in the top right.

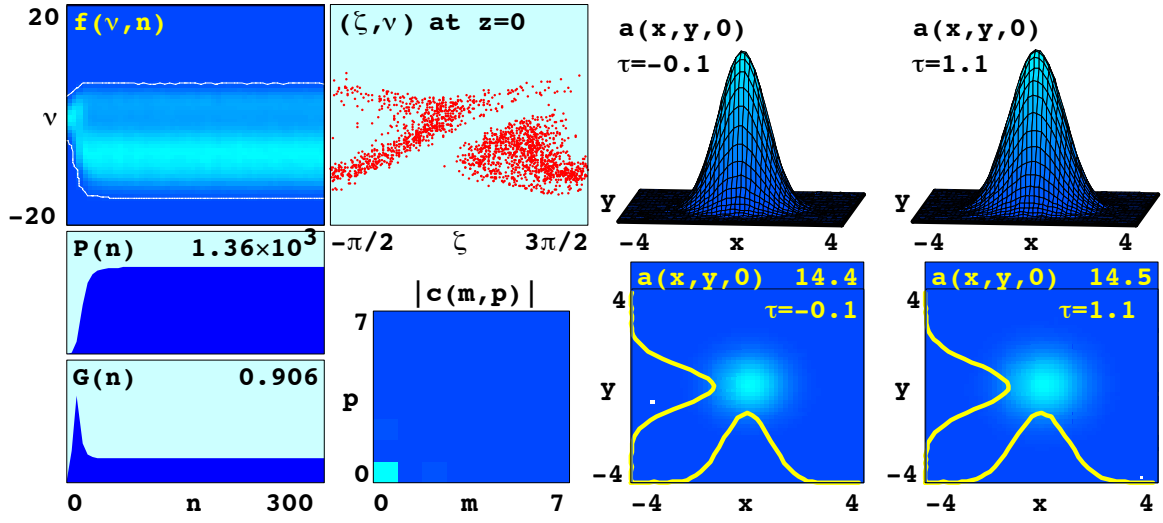


Figure 3.2: Second sample graphical output from 4D model.

THIS PAGE INTENTIONALLY LEFT BLANK

CHAPTER 4:

Design of High Power FELs

In 2013, the DE group at NPS published an article [16] discussing the design requirements for an FEL to reach an average power of 1 MW. The DE group initially started with a requirement for an optical wavelength $\lambda \sim 1 \mu\text{m}$ (chosen for atmospheric propagation). Using a commercially available undulator with a period $\lambda_0 \sim 3 \text{ cm}$ and an undulator parameter $K \sim 1$ provides the required wavelength with an electron beam energy $E_b \sim 100 \text{ MeV}$ (determined using (2.3)). A superconducting, RF (SRF) linac can accelerate electrons with an accelerating gradient of $\sim 10 \text{ MeV/m}$ which gives an accelerator length of $\sim 10 \text{ m}$. FELs have a typical extraction $\eta \sim 2\%$, which means that the required average electron beam power is $P_b \sim 50 \text{ MW}$. Combining that with the electron beam energy gives a required average current $I_{avg} \sim 0.5 \text{ A}$; this can be achieved with a bunch charge $q_b \sim 1 \text{ nC}$ at a pulse repetition frequency of 500 MHz. To achieve good gain, the peak current needs to be $I_{pk} = q_b/t_b \sim 1 \text{ kA}$, which gives a bunch length $t_b \sim 1 \text{ ps}$. For an oscillator, the extraction is approximately $\eta \sim 1/2N$, which requires $N \sim 25$ to achieve an extraction $\eta \sim 2\%$, producing an undulator that is $\sim 0.75 \text{ m}$ long. Most of the design parameters discussed here have been achieved in laboratory FELs, but not all at the same time in a single FEL. For example, a few electron guns have produced nC bunch charges, but not at the high repetition rate listed here, so their average current is much less than the goal of $\sim 0.5 \text{ A}$. This is an important area of research to achieve a high-power FEL.

Previous work at NPS [17] analyzes the robustness of both an oscillator and amplifier FEL by varying emittance ($\epsilon_{x,y}$), energy spread ($\Delta\gamma/\gamma$), mirror shift (Δy_m), and mirror tilt ($\Delta\theta_m$). The Jefferson Laboratory 14 kW FEL was also analyzed for comparison. This thesis work focuses on the oscillator FEL and builds upon the previous work at NPS. Normalized emittance is defined as the phase space area of the electron bunch given by $\epsilon_{x,y} = \gamma \Delta r_{x,y} \Delta \theta_{x,y}$ where $\Delta r_{x,y}$ is the rms transverse position spread of the electron bunch and $\Delta \theta_{x,y}$ is the rms angular spread of the electron bunch, as shown in Figure 4.1 [18]. The energy spread refers to the spread in energies of the individual electrons in the electron bunch. A typical accelerator produces an energy spread $\Delta\gamma/\gamma \sim 0.1\% \rightarrow 1\%$.

The mirror shift and tilt refer to misalignments of the outcoupling mirror, which could be due to platform vibrations for a ship-based FEL. The shift is simulated by moving the mirror up (shifting the center of the optical beam from the middle of the mirror toward the bottom) and the tilt is simulated by rotating the mirror about the center point, which can be seen in Figures 4.2 and 4.3, respectively. The mirror shift is given in μm and the tilt is given in μrad . The mirror shift and tilt could be limited to these magnitudes using active alignment.

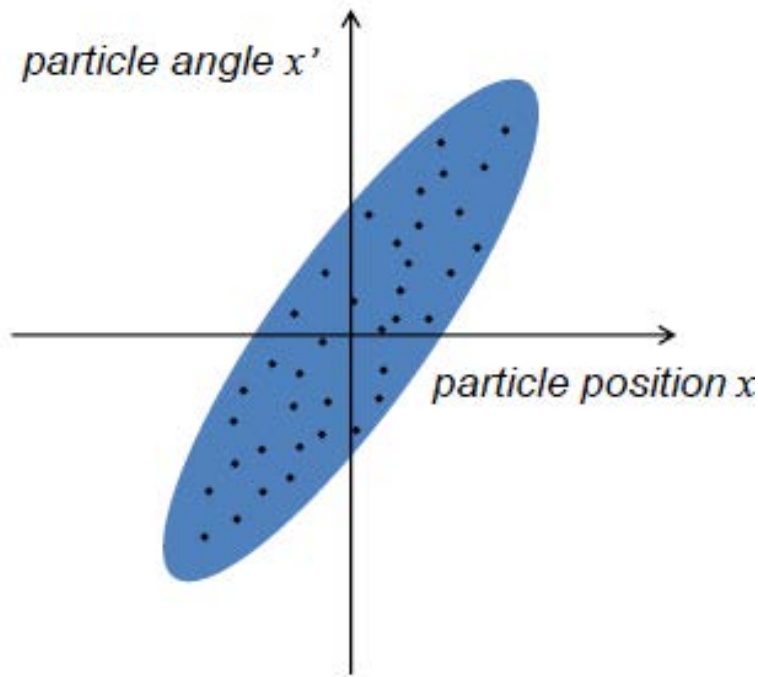


Figure 4.1: Emittance is defined by the area of the electron bunch in phase space, particle angle (x') versus particle position (x), from [18]

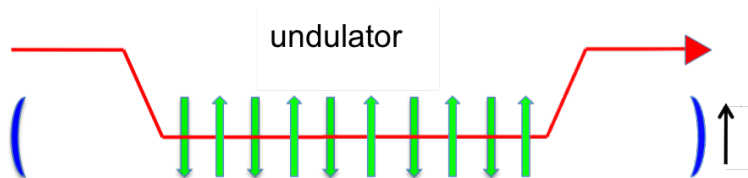


Figure 4.2: Mirror Shift (Δy_m)

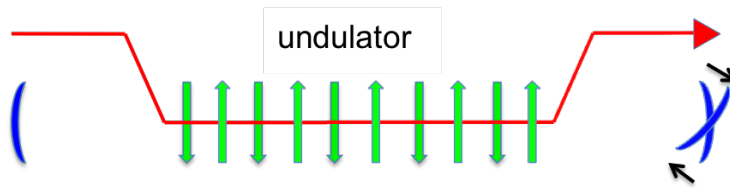


Figure 4.3: Mirror Tilt ($\Delta\theta_m$)

THIS PAGE INTENTIONALLY LEFT BLANK

CHAPTER 5:

Results

5.1 Jefferson Laboratory FEL

The Jefferson Laboratory 14 kW FEL was modeled using both the 2D and 4D programs and the specific parameters shown in Table 5.1. This FEL was chosen to be modeled because the DE group at NPS has previously worked with the team at Jefferson Laboratory and has done numerous models of the 14 kW FEL, with the exception of using the recently developed 4D program. Many experimental results for this FEL have been measured and published; however, a desynchronism curve was never established. This does not allow a comparison of the modeling results with the experimental results. However, an examination of the modeling results does provide an opportunity to visit an issue discovered by Benson in 1985, when he showed that the width of the desynchronism curve using a computer model was twice the length of the experimental desynchronize curve [19].

Figure 5.1 shows the desynchronism curve for the Jefferson Laboratory 14 kW FEL using both the 2D and 4D programs. The 2D results are in blue and the 4D results are in red. The experiment achieved a peak extraction of $\eta \approx 1.4\%$ which compares well with both of the curves, but the 2D curve is approximately half the width of the 4D curve. This mirrors the issue described by Benson where the 4D curve presumably represents the experimental data. Closer examination of the 4D curve shows that the optical wavefront at the point of peak extraction ($d = 0.02$) is 96% in the fundamental cavity mode. Figure 5.2 shows the electron pulse (in red) and the optical field amplitude (in blue) versus z at $x = y = 0$ and the 2D representation of the optical wavefront at the right mirror at a larger desynchronism $d = 0.02$. An examination of the optical wavefront at $d = 0.2$ shows that it is now only 66% in the fundamental mode, as shown in Figure 5.3.

Electron Beam:	
Energy	$E_b = 115 \text{ MeV}$
Bunch Charge	$q = 0.114 \text{ nC}$
Bunch Length (FWHM)	$t_b = 0.4 \text{ ps}$
Peak Current	$I_{peak} = 285 \text{ A}$
Normalized Transverse Emittance (rms)	$\epsilon_{x,y} = 8 \text{ } \mu\text{m}$
Energy Spread (rms)	$\Delta\gamma/\gamma = 0.4\%$
Undulator:	
Period	$\lambda = 5.5 \text{ cm}$
Length	$L = 1.65 \text{ m}$
Undulator Parameter	$K = 1.36$
Optical Cavity:	
Wavelength	$\lambda = 1.6 \text{ } \mu\text{m}$
Cavity Length	$S = 32 \text{ m}$
Rayleigh Length	$Z_0 = 75 \text{ cm}$
Quality Factor	$Q_n = 5$
Mirror Radius	$R_{mir} = 3.8 \text{ cm}$

Table 5.1: Jefferson Laboratory FEL Oscillator Parameters, from [17]

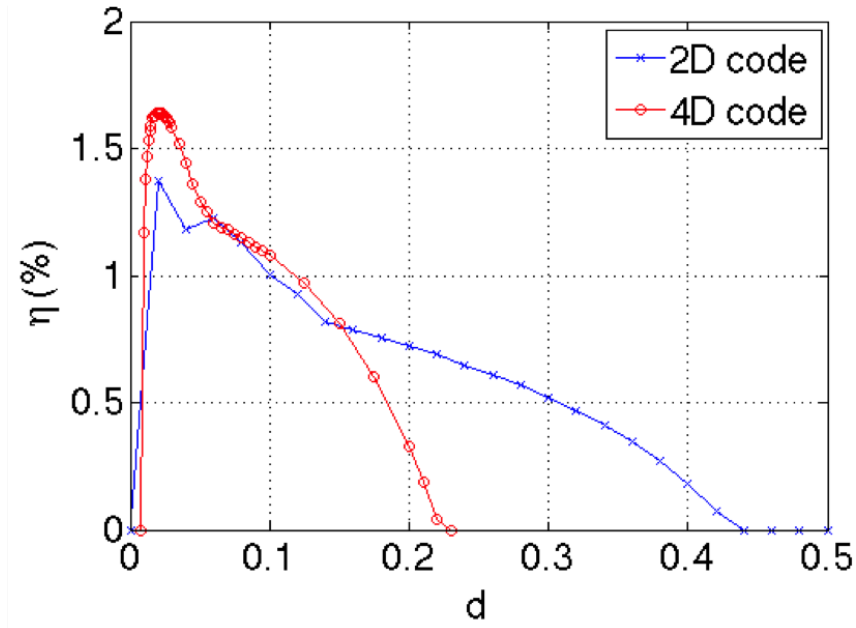
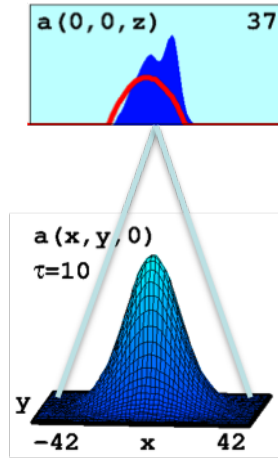
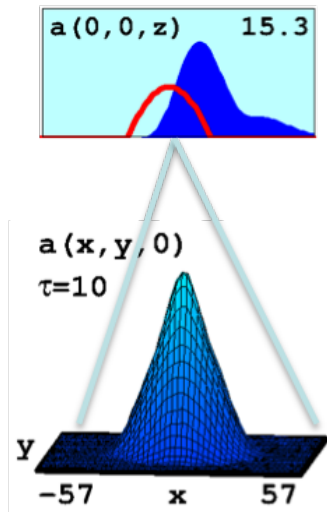


Figure 5.1: Modeled desynchronism curve (extraction η versus dimensionless desynchronism value d) for Jefferson Laboratory 14 kW FEL using the NPS 2D model (blue) and the new 4D model (red)



96% in cavity fundamental mode

Figure 5.2: Optical wavefront depiction for $d = 0.02$. Top: optical amplitude $|a|$ versus z at $x = y = 0$. Bottom: optical amplitude $|a|$ versus (x, y) at $z = 0$



66% in cavity fundamental mode

Figure 5.3: Optical wavefront depiction for $d = 0.2$. Top: optical amplitude $|a|$ versus z at $x = y = 0$. Bottom: optical amplitude $|a|$ versus (x, y) at $z = 0$

The 2D program assumes that the optical wavefront stays in the fundamental mode, which leads to the initial conclusion that the difference between the curves is due to the change in optical wavefront mode. Various things can change the mode of an optical wavefront in a cavity, including mirror imperfections and mirror clipping. Additionally, gain distortion can cause the mode to change [14]. The 2D and 4D model runs assumed zero mirror imperfections. Also, the mirror radius used for the modeling was sufficient to prevent significant clipping from occurring. One difference between the 2D and 4D models is that the 2D model assumes that the optical wavefront stays in the fundamental mode and the 4D model allows the optical wavefront to operate in higher-order modes. This leads to the hypothesis that the mode of the optical wavefront plays a role in the width of the desynchronism curve. To verify this conclusion the desynchronism curve was generated again, except the 4D parameters were adjusted so that the simulated optical cavity prevented the higher order modes from experiencing significant gain.

Figure 5.4 shows the new desynchronism curve where the 2D and 4D curves are now aligned. Investigating the optical wavefront at $d = 0.02$ and $d = 0.2$ shows that the optical wavefront now stays in the fundamental mode (99% and 97%, respectively), shown in Figures 5.5 and 5.6. These results support the conclusion that the change in mode causes the model desynchronism curve to be twice as long as a curve where the optical wavefront stays in the fundamental mode.

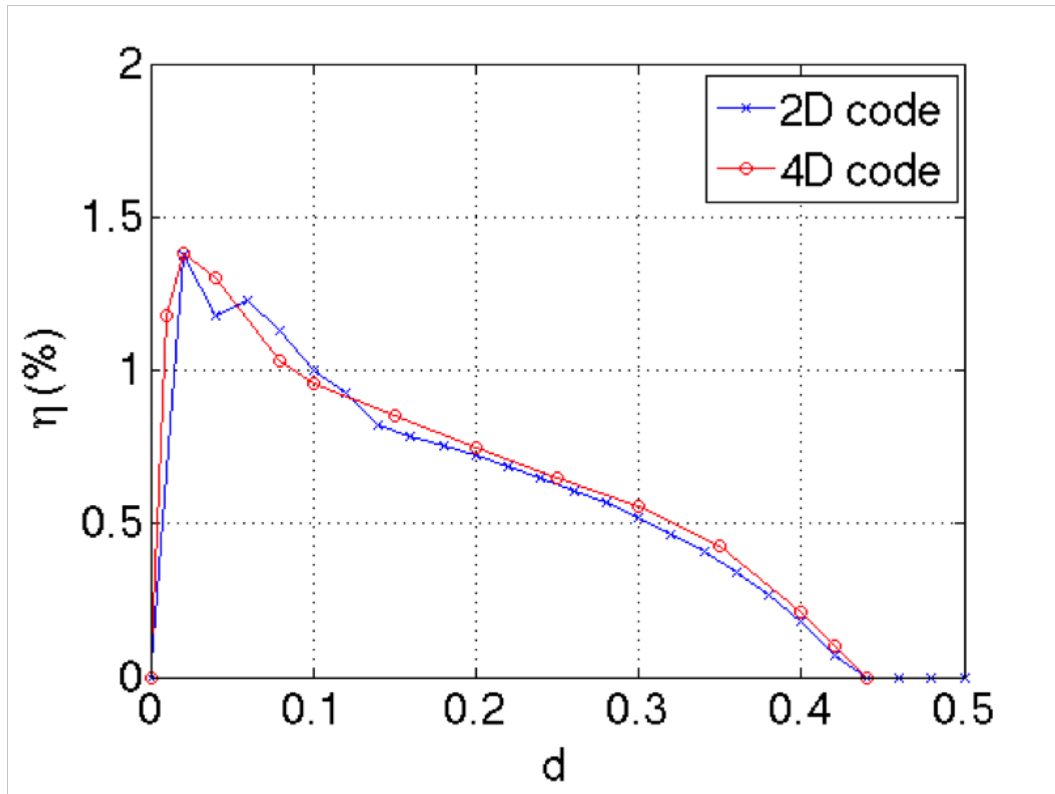
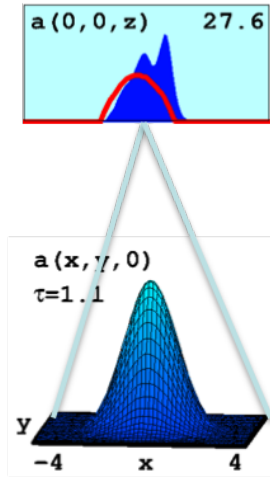
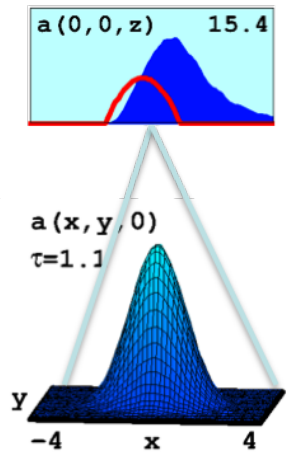


Figure 5.4: Adjusted desynchronism curve for Jefferson Laboratory 14 kW FEL. For the 4D model (red), the cavity mirrors are now positioned just outside the undulatory, forcing the optical wavefront to remain primarily in the fundamental mode



99% in cavity fundamental mode

Figure 5.5: Adjusted optical wavefront depiction for $d = 0.02$. Top: optical amplitude $|a|$ versus z at $x = y = 0$. Bottom: optical amplitude $|a|$ versus (x, y) at $z = 0$



97% in cavity fundamental mode

Figure 5.6: Adjusted optical wavefront depiction for $d = 0.2$. Top: optical amplitude $|a|$ versus z at $x = y = 0$. Bottom: optical amplitude $|a|$ versus (x, y) at $z = 0$

Electron Beam:	
Energy	$E_b = 44.3 \text{ MeV}$
Bunch Charge	$q = 5 \text{ pC}$
Bunch Length (FWHM)	$t_b = 2.9 \text{ ps}$
Peak Current	$I_{peak} = 1.85 \text{ A}$
Normalized Transverse Emittance (rms)	$\epsilon_{x,y} = 8.8 \text{ } \mu\text{m}$
Energy Spread (rms)	$\Delta\gamma/\gamma = 0.1\%$
Undulator:	
Period	$\lambda = 3.3 \text{ cm}$
Length	$L = 4.95 \text{ m}$
Undulator Parameter	$K = 0.709$
Optical Cavity:	
Wavelength	$\lambda = 3.3 \text{ } \mu\text{m}$
Cavity Length	$S = 12.68 \text{ m}$
Rayleigh Length	$Z_0 = 271.2 \text{ cm}$
Quality Factor	$Q_n = 66.7$
Mirror Radius	$R_{mir} = 2 \text{ cm}$

Table 5.2: Stanford FEL Oscillator Parameters, from [19]

5.2 Stanford FEL

The Stanford FEL was chosen to be modeled with the 2D and 4D programs since it was the FEL that Benson used in his research where he discovered the discrepancies between experimental data and modeling results, as previously discussed. The parameters used are shown in Table 5.2. Figure 5.7 shows the desynchronism curve with the 2D program in blue and the 4D program in red and Figure 5.8 shows the experimental desynchronism curve.

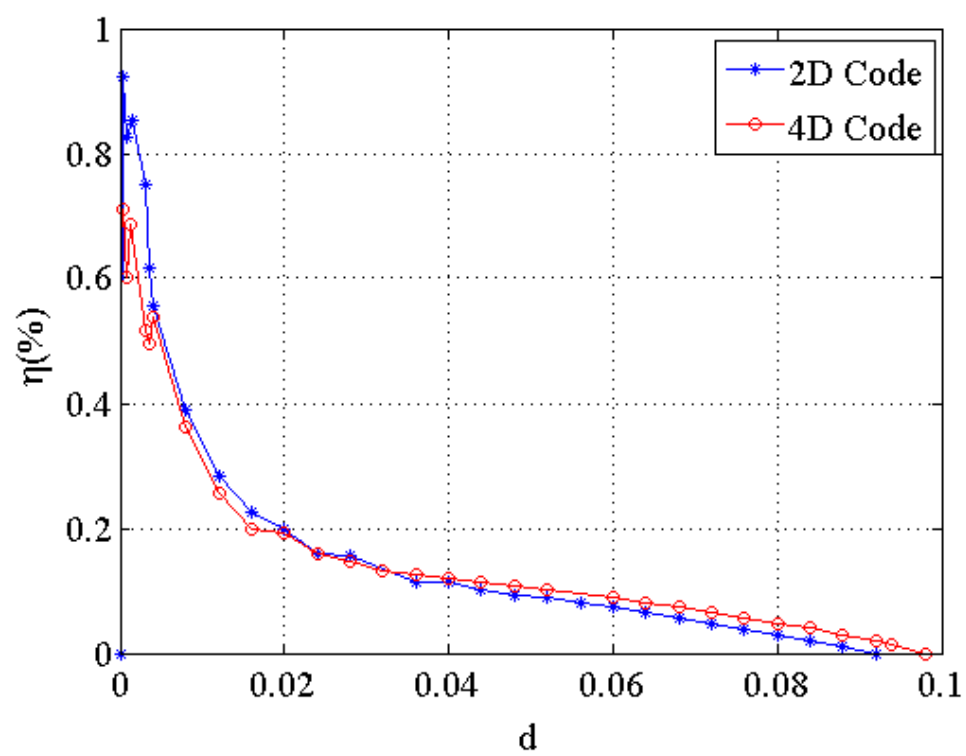


Figure 5.7: Modeled desynchronism curve for Stanford FEL

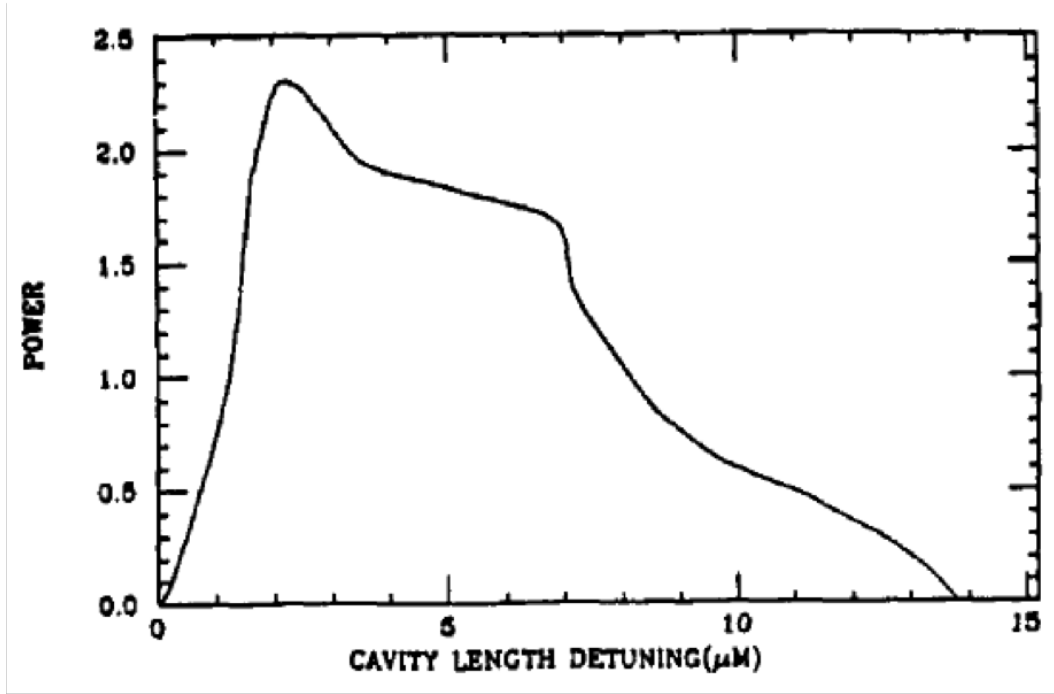
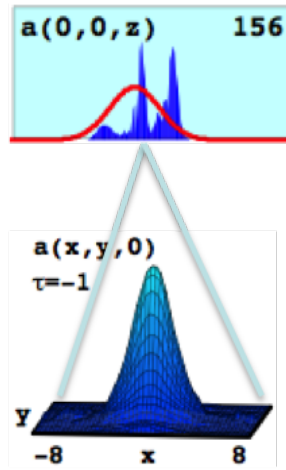


Figure 5.8: Experimental desynchronism curve for Stanford FEL, from [19]

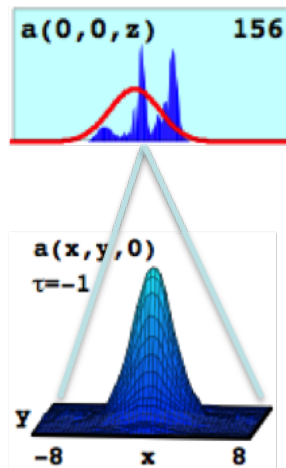
As can be seen in Figure 5.7, the 2D and 4D programs match and give an approximate width of $d = 0.09$ for the desynchronism curve. Analysis of the optical wavefronts, as seen in Figures 5.9 and 5.10, shows that it stays primarily in the fundamental mode from $d = 0.0004$ (100% in the fundamental mode) to $d = 0.06$ (99% in the fundamental mode). This is further verification of the conclusion made in the last section regarding diffraction and the correlation between the optical mode and the width of the desynchronism curve. The width of the experimental desynchronism curve in Figure 5.8 corresponds to dimensionless desynchronism $d \sim 0.06$, according to (2.28). This width is shorter than the width of the modeled desynchronism curve; however, it is on the order of half the width of the modeled curve reported by Benson [19]. The discrepancy between the experimental curve and the NPS modeled curve may be due to the fact that the parameters of the electron beam were slightly different than that reported by Benson; it may also indicate, based upon the analysis of the previous section, that the Stanford experiment had higher order optical content present in significant amounts. However, the NPS code does come significantly

closer than previous modeling in predicting the width of the desynchronism curve.



100% in cavity fundamental mode

Figure 5.9: Optical wavefront depiction for $d = 0.004$



100% in cavity fundamental mode

Figure 5.10: Optical wavefront depiction for $d = 0.06$

5.3 Emittance Versus Energy Spread

To better understand the robustness of the design of a notional higher power FEL oscillator, modeling was used to estimate the tolerances of the emittance and energy spread of the electron beam while still maintaining a decent value of extraction. The parameters of the notional oscillator is shown in Table 5.3.

Figure 5.11 shows a 3D graph of extraction (η) versus transverse emittance ($\epsilon_{x,y}$) and energy spread ($\Delta\gamma/\gamma$). The peak extraction achieved is 2.7%; however, as seen in Figure 5.11, this value is only achievable at an emittance of $5\mu\text{m}$ and an energy spread of $0\% - 0.4\%$. Once either is above these respective levels, the extraction has a significant drop off and then a more general, and predictable, downward trend.

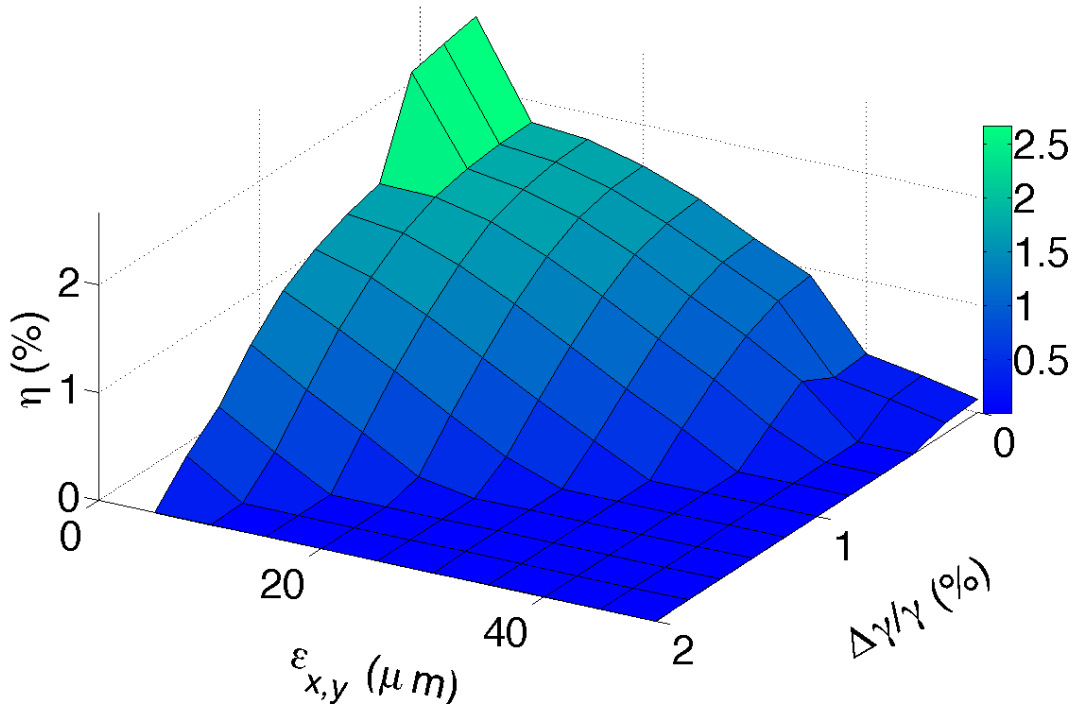


Figure 5.11: Extraction (η) for emittance ($\epsilon_{x,y}$) versus energy spread ($\Delta\gamma/\gamma$) for a generic oscillator

Focusing on the sharp jump in extraction shows some interesting behavior with regard to

Electron Beam:	
Energy	$E_b = 120 \text{ MeV}$
Bunch Charge	$q = 1 \text{ nC}$
Bunch Length (FWHM)	$t_b = 2 \text{ ps}$
Peak Current	$I_{peak} = 500 \text{ A}$
Undulator:	
Period	$\lambda = 3 \text{ cm}$
Length	$L = 0.75 \text{ m}$
Undulator Parameter	$K = 1.8$
Optical Cavity:	
Wavelength	$\lambda = 1.1 \mu\text{m}$
Cavity Length	$S = 20 \text{ m}$
Rayleigh Length	$Z_0 = 7.5 \text{ cm}$
Quality Factor	$Q_n = 4$
Mirror Radius	$R_{mir} = 8 \text{ cm}$

Table 5.3: Generic FEL Oscillator parameters, from [17]

the optical wavefront. Figures 5.12 and 5.13 show the transverse profile of the electron pulse and optical field amplitude in the x direction at the beginning of the undulator and the evolution of the optical power spectrum at the pulse center for $\epsilon_{x,y} = 10 \mu\text{m}$ and $5 \mu\text{m}$, respectively, with $\Delta\gamma/\gamma = 0\%$ in both cases. Examining Figure 5.12 shows that the FEL reaches steady state with an extraction of 1.7%. The optical wavefront is a Gaussian. When the emittance is changed to $5 \mu\text{m}$, the FEL finds a new mode of operation before it reaches steady state. Comparing Figures 5.12 and 5.13 shows this new transverse mode. The optical field amplitude profile has developed a double peak and the optical power spectrum shifts to the new mode prior to reaching steady state. This new mode dramatically increases the extraction (now 2.7%). This new mode of operation is not seen past an energy spread of 0.4% and an emittance of $5 \mu\text{m}$ which suggests that if the emittance and energy spread of the electron beam can be maintained below these limits, then extraction will see a significant increase. While these results suggest a behavior, experiments are required to verify the modeling results and determine the implications of the new operating mode.

One explanation for the increase in extraction is that for the lower emittance, the electron pulse has a higher peak current at the center, which can be seen when comparing Figures 5.12 and 5.13. This higher peak current will increase the gain of the optical pulse on

axis, which introduces mode distortion by placing optical power into higher order gaussian modes. This allows the cavity to store additional power in higher order modes rather than the fundamental, while reducing the on axis optical intensity along the undulator, perhaps delaying the onset of saturation. While the behavior provides an extra percent of extraction, it results in worse beam quality. When designing an FEL, that will need to be taken into consideration.

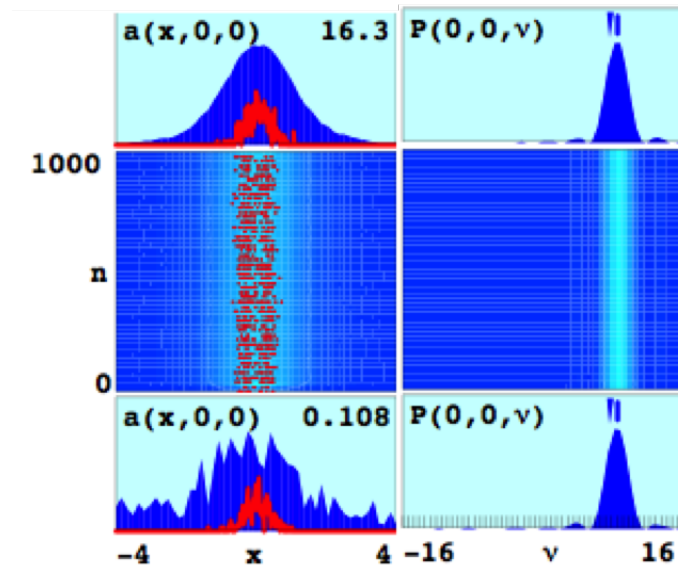


Figure 5.12: Optical field amplitude and optical power spectrum for $\varepsilon_{x,y} = 10\mu\text{m}$ and $\Delta\gamma/\gamma = 0\%$

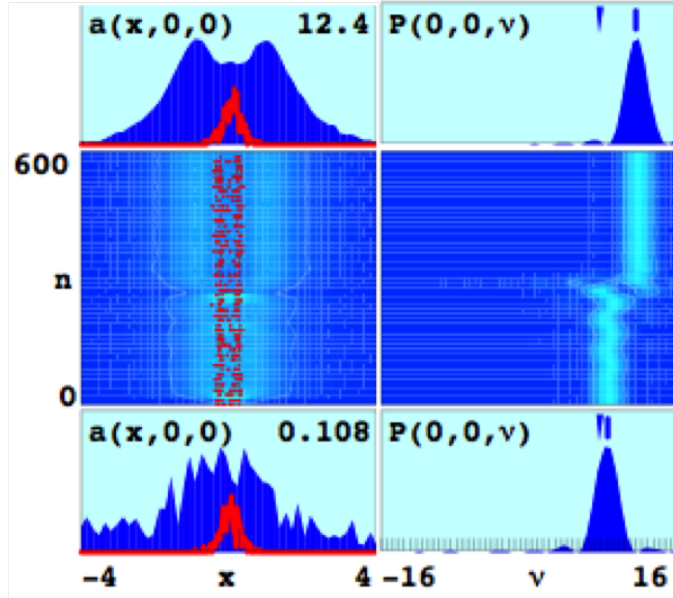


Figure 5.13: Optical field amplitude and optical power spectrum for $\varepsilon_{x,y} = 5\mu\text{m}$ and $\Delta\gamma/\gamma = 0\%$

5.4 Mirror Shift and Tilt

To better understand the design requirements for a FEL that will experience shipboard conditions, modeling was used to determine the effects of adjusting the mirror shift (Δy_m) and mirror tilt ($\Delta\theta_m$) on extraction. Previous work at NPS has shown that an FEL will be subjected to large scale but low frequency vibrations (due to waves and sea state) and smaller, higher frequency vibrations (due to onboard machinery) [20]. The larger vibrations can be accounted for using active damping that is commercially available. The smaller, high frequency vibrations are more difficult to mitigate actively and can become a problem. The parameters in Table 5.3 were used with an emittance of $10\mu\text{m}$ and an energy spread of 0.2%. The peak extraction is 1.7% and the results, as seen in Figure 5.13, show that at least half of that extraction can be achieved for $\Delta y_m \leq 30\mu\text{m}$ and $\Delta\theta_m \leq 2\mu\text{rad}$. It is believed by experimentalists that the vibrations that are experienced during shipboard conditions can be actively damped down to support the mirror shifts and tilts to maintain half of the peak extraction for the modeled FEL.

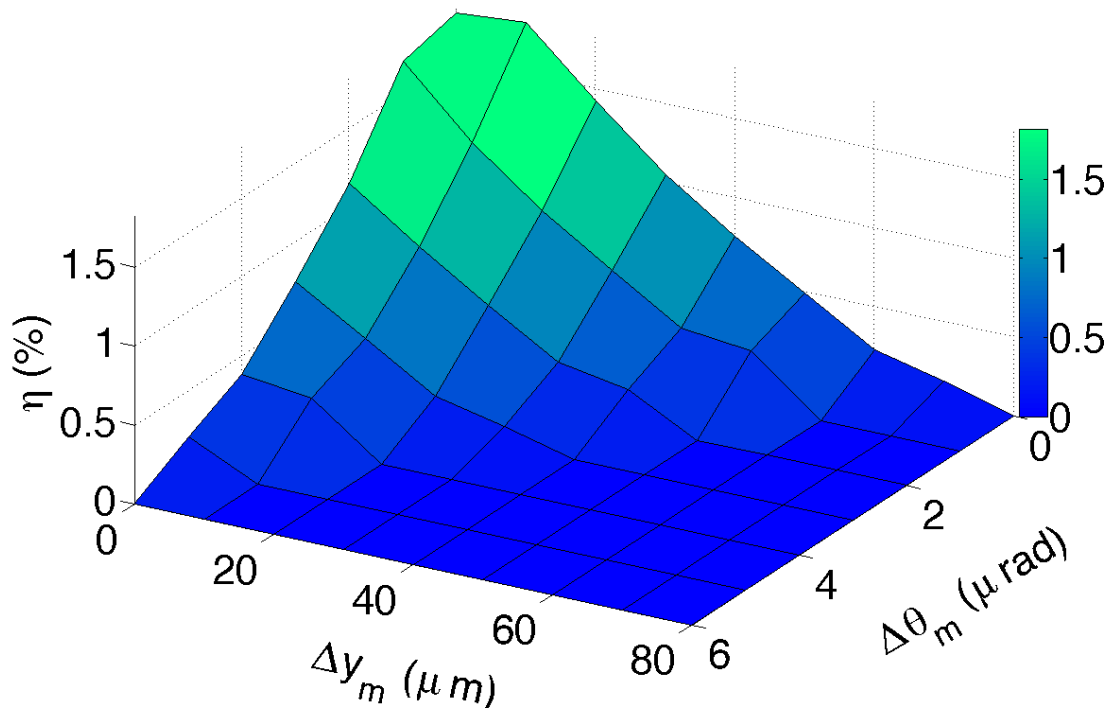


Figure 5.14: Extraction (η) for mirror shift (Δy_m) versus mirror tilt ($\Delta \theta_m$) for a generic oscillator

THIS PAGE INTENTIONALLY LEFT BLANK

CHAPTER 6:

Conclusion

Analysis of desynchronism curves using the 2D and 4D models shows that the model curves are longer than experimental curves when the optical wavefront stays in the fundamental mode. There exist a few possibilities as to the cause of this: the combined effects of diffraction and gain distortion, the basis set for the optical modes, and the relative lengths of the gain medium and the optical cavity. In order to better understand this issue, more modeling runs would be required as well as experiments that simultaneously measure the desynchronism curve and the modal composition.

The 4D simulation results used to determine the robustness of a FEL design showed that there exists a new transverse mode that develops for a normalized emittance $\epsilon_{x,y} = 5 \mu\text{m}$ and energy spread $\Delta\gamma/\gamma \leq 0.4\%$. Future work should involve the determination of how this new mode develops as well as experimental verification. If this new mode is observed experimentally, then it could enable a significant increase in the extraction and will help focus the efforts of FEL design to achieve the required electron beam parameters.

Simulation results also show that at least half of the maximum extraction can be achieved with a mirror shift $\Delta y_m \leq 30 \mu\text{m}$ and mirror tilt $\Delta\theta_m \leq 2 \mu\text{rad}$. These results show the robustness of the FEL design with regard to mirror alignment. Further work should focus on expected misalignments due to vibrations in a realistic shipboard environment. Once that is determined, active mirror alignment systems should be examined to improve FEL performance.

Modeling continues to provide valuable insight into the design of FELs as well as the dynamic physics of FEL operation. Continued modeling will be required to further advance FEL technology and understanding in order to achieve high powers for operational use.

THIS PAGE INTENTIONALLY LEFT BLANK

List of References

- [1] L. R. Elias *et al.*, “Observation of stimulated emission of radiation by relativistic electrons in a spatially periodic transverse magnetic field,” *Physical Review Letters*, vol. 36, no. 13, pp. 717–720, 1976.
- [2] J. M. J. Madey, “Stimulated emission of bremsstrahlung in a periodic magnetic field,” *Journal of Applied Physics*, vol. 42, no. 1, pp. 1906–1913, 1971.
- [3] H. Motz, “Applications of the radiation from fast electron beams,” *Journal of Applied Physics*, vol. 22, no. 5, pp. 527–535, 1951.
- [4] H. Motz, W. Thon, and R. N. Whitehurst, “Experiments on radiation by fast electron beams,” *Journal of Applied Physics*, vol. 24, no. 7, pp. 826–833, 1953.
- [5] D. A. G. Deacon *et al.*, “First operation of a free-electron laser,” *Physical Review Letters*, vol. 38, no. 16, pp. 892–894, 1977.
- [6] P. van Amersfoort, “First lasing with FELIX,” *Nucl. Instr. Meth. Phys. Res. Section A*, vol. A318, p. 4246, 1992.
- [7] P. Michel *et al.*, “First lasing of the elbe mid-IR FEL,” in *Proc. of the 2004 FEL Conference*, Trieste, Italy, August 2004, pp. 8–13.
- [8] D. Dunning *et al.*, “First lasing of the ALICE IR-FEL at Daresbury Laboratory,” in *Proc. of FEL2011*, Shanghai, China, August 2011, pp. 1–4.
- [9] D. Douglas *et al.*, “A 10kw IRFEL design for Jefferson lab,” in *Proc. of the 2001 Particle Accelerator Conference*, Chicago, USA, June 2004, pp. 249–252.
- [10] C. on a Scientific Assessment of Free-Electron Laser Technology for Naval Applications and T. N. R. Council, “Scientific assessment of high-power free-electron laser technology,” National Research Council of the National Academies, Tech. Rep., 2009.
- [11] C. R. Fussman, “High energy laser propagation in various atmospheric conditions utilizing a new, accelerated scaling code,” master’s thesis, Naval Postgraduate School, 2014.
- [12] W. Colson and A. Renieri, “Pulse propagation in free electron lasers,” *Journal de Physique Colloques*, vol. 44, no. C1, pp. C1–11–C1–27, 1983.

- [13] G. Dattoli *et al.*, “Lethargy of laser oscillations and supermodes in free-electron lasers. ii. quantitative analysis,” *Physical Review Letters A*, vol. 37, no. 11, pp. 4334–4339, 1988.
- [14] W. Colson, C. Pellegrini, and A. Renieri, Eds., *Free Electron Laser Handbook*. The Netherlands: North-Holland Physics, 1990.
- [15] J. Blau *et al.*, “Four-dimensional simulations of free electron laser amplifiers and oscillators,” 2015, to Be Published in the Proceedings of the 2015 FEL Conference.
- [16] J. Blau *et al.*, “High average power free-electron lasers,” *Optical Engineering*, vol. 52, no. 2, pp. 021 013–1–021 013–8, 2013.
- [17] J. Blau *et al.*, “Electron beam quality and alignment effects in free electron laser amplifiers and oscillators,” 2015, unpublished.
- [18] H. Braun. Emittance diagnostics. [Online]. Available: <http://cas.web.cern.ch/cas/France-2008/Lectures/Braun-Emittance.pdf>.
- [19] S. V. Benson, “Diffractive effects and noise in short pulse free-electron lasers,” Ph.D. dissertation, Stanford University, 1985.
- [20] J. A. Beauvais, “FEL mirror response to shipboard vibrations,” master’s thesis, Naval Postgraduate School, 2011.

Initial Distribution List

1. Defense Technical Information Center
Ft. Belvoir, Virginia
2. Dudley Knox Library
Naval Postgraduate School
Monterey, California